

Competing magnetic interactions and emergent phase diagrams in double perovskite $Y_2Ni_xCo_{1-x}MnO_6$

Richa Pokharel Madhogaria¹, Nicholas S. Bingham², Raja Das³, Manh-Huong Phan^{1,*},
and Hariharan Srikanth^{1,*}

¹ Department of Physics, University of South Florida, Tampa, Florida 33620, USA

² Department of Applied Physics, Yale University, New Haven, Connecticut 06511, USA

³ Faculty of Materials Science and Engineering, Phenikaa University, Yen Nghia, Ha Dong,
Hanoi 12116, Vietnam

Abstract

We present a comparative study of double perovskites $Y_2Ni_xCo_{1-x}MnO_6$ for $x = 1, 0.5,$ and 0 . The polycrystalline samples of $Y_2Ni_xCo_{1-x}MnO_6$ with space group $P2_1/n$ were synthesized via *sol-gel* technique. X-ray photoelectron spectroscopy (XPS) confirms the presence of majority Ni^{2+}/Mn^{4+} in Y_2NiMnO_6 (YNMO) and a mixed valence state $Ni^{2+/3+}/Co^{2+/3+}/Mn^{4+/3+}$ in co-doped $Y_2Ni_{0.5}Co_{0.5}MnO_6$ (YNCMO). The temperature dependent magnetization results suggest homogeneous substitution of Ni ions with Co ions with minimal contribution of 3+ cationic magnetic interactions in YNCMO. The superexchange ferromagnetic (FM) interaction has a major contribution to the magnetism of YNMO. The strength of antiferromagnetic (AFM) coupling resulting from the antiphase boundaries in $Y_2Ni_xCo_{1-x}MnO_6$ increases with the increase in the Co concentration. The AC susceptibility ($AC-\chi$) study further validates the presence of higher density of antiphase boundaries, which is reflected by the dynamics of domain walls in YNCMO. The isothermal magnetic entropy change (ΔS_M) as functions of temperature and magnetic field is exploited to assess the stabilization of different magnetic phases. The findings

of $\Delta S_M(T, \mu_0 H)$ lead to the proposed new magnetic phase diagrams for $Y_2Ni_xCo_{1-x}MnO_6$ for $x = 1$ and 0.5 , in comparison with the previously established phase diagram of Y_2CoMnO_6 .

KEYWORDS: Double perovskites; Collective Magnetism; Magnetocaloric Effect; Magnetic Phase Diagram

*Corresponding authors: phanm@usf.edu (M.H.P.); sharihar@usf.edu (H.S.)

1. Introduction

Double perovskite oxides have generated a growing interest in the scientific community due to their outstanding properties with composition variations [1-3]. Among them R_2NiMnO_6 (RNMO), where R is a rare-earth ion, are ferromagnetic (FM) semiconductor oxides involving rich physics. The multifunctional RNMO exhibits various properties such as ferromagnetism/antiferromagnetism, magnetodielectricity, magnetoresistance, magnetocapacitance, giant magnetocaloric effect [4-6] which can be tailored via external electric and magnetic fields, making them promising candidates for spintronics applications. The crystal structure of RNMO is dependent on the occupancy of the Ni and Mn atoms at the crystallographic sites. The alternating arrangement of the Ni/Mn atoms makes RNMO crystallize into a monoclinic ($P2_1/n$) phase while the random distribution of the transition metal ions in the lattice leads to the orthorhombic ($Pbnm$) phase [5]. The rhombohedral ($R3c$ or $R3m$ or $R3$) phase has also been observed in RNMO for $R = La$ [7]. The magnetic properties of RNMO are governed by the Goodenough-Kanamori rules, with FM coupling arising from a 180° superexchange interaction between two transition metal cations [5][6][8]. In addition to the B -site ions (Ni/Mn), the size of the R cation plays an important role in identifying the magnetism of RNMO. The density functional theory (DFT) calculation shows that the replacement of $R = La /$

Sm by $R = Y$ would change the magnetic order in the system from FM to E*-type antiferromagnetic (AFM) [9]. In such a system, the E*-type structure results in breaking of inversion symmetry, giving rise to the ferroelectric behavior. In contrast to the theoretical prediction, an experimental study for different R^{3+} ions did not realize the E*-type structure leading to breaking of inversion symmetry in RNMO [10-11]. The R^{3+} ions also have a strong influence on the magnetic transition temperature. A study conducted by Retuerto *et al.* showed that the paramagnetic (PM) – FM ordering temperature (Curie temperature) reduces with the reduction in size of the rare-earth ions [7]. The magnetic exchange interactions in RNMO are largely associated with the octahedral tilting, Ni/Mn – O bond lengths and bond angles between Ni – O – Mn [4-7]. R_2CoMnO_6 (RCMO), where Ni ion is replaced by Co ion, are sister compounds whose properties are also equally governed by the rare-earth ions. In RCMO, the magnetic ground state for $R = Ho / Tm$ is FM, while for $R = Yb / Lu$ competitive interactions lead to the E -type arrangement [12]. In the same study, the authors suggested that substitution of R^{3+} ions with smaller ionic radius could lead to comparatively more structural distortion, giving rise to the enhanced competitive interactions between the nearest neighbor (FM) and next nearest neighbor (AFM) which stabilize the E phase in such systems.

Among the sister compounds, Y_2CoMnO_6 (YCMO) and Y_2NiMnO_6 (YNMO), the E-type magnetic ground state has been predicted theoretically [9][13], however, many experimental studies have shown either FM or canted spin structure [10][11][14]. YCMO and YNMO crystallize into the monoclinic space group $P2_1/n$ at room temperature. Both compounds have been reported as multiferroic materials where the ferroelectricity has been attributed to the exchange striction in the E-type magnetic structure. It was argued by Blasco *et al.* that the

pyroelectric behavior in YCMO was due to the thermally stimulated polarization current rather than the ferroelectric effect [14].

As stated above, the magnetism in YCMO and YNMO is guided by the superexchange interaction between the transition metal ions, $\text{Mn}^{4+}\text{-O}^{2-}\text{-Co}^{2+}$ and $\text{Mn}^{4+}\text{-O}^{2-}\text{-Ni}^{2+}$, giving rise to the FM coupling. The presence of the same R^{3+} ion and with only a slight difference in the r_B , the average atomic radii of *B*-site cations, gives rise to almost similar PM–FM transition temperature in these compounds. Depending upon the synthesis route, the T_C for these systems has been reported to vary in the range of 75 – 85 K [15-17]. Apart from the FM ordering originating from the virtual hopping of electrons between half-filled $\text{Ni}^{2+}/\text{Co}^{2+}$ orbital and the empty Mn^{4+} orbital, the competitive AFM exchange interactions such as $\text{Mn}^{4+}\text{-O-Mn}^{4+}$ or $\text{Co}^{2+}\text{-O-Co}^{2+}$ or $\text{Ni}^{2+}\text{-O-Ni}^{2+}$ also occur [14][15]. The latter is the consequence of the presence of the antisite disorder/antiphase boundaries where the *B*-site cations interchange their positions resulting in the above-mentioned exchanges. The presence of the AFM coupling in these compounds reduces the long-range FM ordering. In YCMO, the occurrence of the significant antiphase has been shown to impact the ground state magnetism. The magnetic jumps observed in the field dependent magnetization curves in YCMO has been associated with the pinning of magnetic domain walls by the Co/Mn rich antiphase boundaries [14][16][18]. On the basis of the steps seen in the M vs. H , YCMO has been defined as a metamagnetic system [15]. Although similar type of interactions are also expected to occur in YNMO, no magnetization steps have been observed with respect to the antiphase boundaries [15]. The decrease in the saturation magnetization in YNMO is mainly attributed to the spin canting with small contribution from the presence of antiphase in YNMO [19].

The presence of disorder introduces antiphase boundaries resulting in AFM coupling in the double perovskites (RNMO and RCMO). Depending upon the size and the electronic stability of *A*-site and *B*-site cations present in the double perovskites different signatures such as metamagnetic jumps in YCMO [11][13][15], glass-like behavior in La₂CoMnO₆ (LCMO) [8] and decrease in the saturation magnetization in the YNMO [15][19], have been observed. In the isostructural compound La₂Ni_xCo_{1-x}MnO₆, the low temperature frequency dependent anomaly in the imaginary part of AC susceptibility seen for $x = 0.2 - 0.8$ has been assigned to the spin glass like state [20]. Since earlier reports indicate the existence of glassiness in both La₂CoMnO₆ [8][20] and La₂NiMnO₆ (LNMO) [20], the glass-like feature in their co-doped compounds is to be expected. However, the evolution of the antiphase and how it changes the magnetic ground state in Y₂Ni_xCo_{1-x}MnO₆ compounds are yet to be addressed. In the present study, we aim to shed light onto the effect of AFM exchange interactions caused due to the antisite disorder in the YNMO and co-doped Y₂Ni_{0.5}Co_{0.5}MnO₆ (YNCMO), in comparison to the YCMO.

2. Experiment

Polycrystalline samples of Y₂NiMnO₆ and Y₂Ni_{0.5}Co_{0.5}MnO₆ were prepared through a conventional sol-gel method. High purity reagent chemicals yttrium nitrate hexahydrate (Y₂Ni₃O₉·6H₂O), cobalt sulphate heptahydrate (CoSO₄·7H₂O) and manganese nitrate tetrahydrate (MnN₂O₆·4H₂O) were taken corresponding to their stoichiometric ratios. Citric acid acting as a chelating agent was added to the solution of the precursors. The resulting mixture was then continuously stirred and heated from 100 – 400 °C until the formation and decomposition of viscous gel was observed. The final product was grounded and calcined at 900 °C for 8 h to obtain the required phase.

The structural phase was confirmed by the x-ray diffraction (XRD) at room temperature using Bruker AXS powder x-ray diffractometer with Cu-K α radiation. The energy dispersive spectroscopy (EDS) was carried out via JEOL JSM-6390LV SEM. X-ray Photoelectron Spectroscopy was performed with a PHI Versa Probe II, in ultra-high vacuum ($\sim 10^{-8}$ torr). Magnetic measurements were done using Quantum Design Physical Property Measurement System (PPMS) with the Vibrating Sample Magnetometer (VSM) and AC Measurement System (ACMS) options. Magnetization versus applied magnetic field (M vs. H) was measured from $H = 0 - 80$ kOe for temperatures ranging from $T = 3 - 100$ K, and magnetization versus temperature was measured from $T = 3 - 120$ K for $H = 0.1 - 20$ kOe. The real and imaginary parts of AC susceptibility were measured simultaneously for $T = 10 - 120$ K for frequencies $f = 10 - 635$ Hz with an AC driving field amplitude $h = 5$ Oe. Magnetic entropy change was calculated from the magnetization versus field data which were measured up to $H = 60$ kOe for $T = 5 - 100$ K for YNMO and $T = 5 - 90$ K for YNCMO. For all the measurements, the field and the temperature scan rates were 20 Oe/s and 3 K/min, respectively.

3. Results and discussion

3.1 Structure and cationic ordering

The room temperature x-ray powder diffraction patterns for YNMO and YNCMO are shown in Figs. 1(a) and (b), respectively. The obtained diffraction peaks for both systems fall into monoclinic $P2_1/n$ space group. The peak at $2\theta = 29^\circ$ in Fig. 1(a) and (b) can be associated with a small portion of Y_2O_3 , which has negligible influence on the magnetism [16]. With the use of Debye Scherrer formula, $\tau = \frac{K\lambda}{\beta \cos \theta}$, where K is the dimensionless shape factor, λ is the wavelength of the X-ray, β is the line broadening at half the maximum intensity and θ is the

Bragg angle, the crystallite size is calculated to be approximately 33 nm for YNMO and 42 nm for YNCMO. According to EDS, the chemical composition of different elements in the samples were found to be: In YNMO 17.4 at% of Y (SD = 2.6), 8.4 at% of Ni (SD = 1.5), 7.5 at% of Mn (SD = 1.6) and 60.9 at% of O (SD = 5.7) is present and YNCMO consists of 21.1 at% of Y (SD = 1.0), 5.2 at% of Ni (SD = 0.6), 5.6 at% of Co (SD = 0.9), 10.2 at% of Mn (SD = 1.3) and 57.8 at% of O (SD = 3.5).

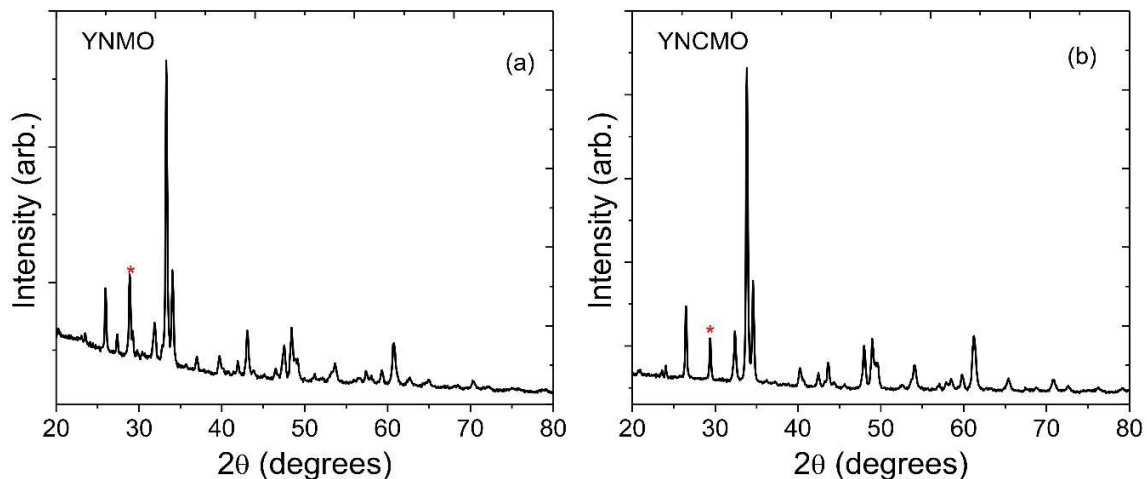


Figure 1 XRD patterns of the polycrystalline (a) YNMO and (b) YNCMO samples. The star represents the peak corresponding to Y_2O_3 .

X-ray photoelectron spectroscopy (XPS) was performed to confirm the valence states of the different magnetic ions involved [Fig. 2]. The CASAXPS software was used to fit the obtained spectrum at the Ni, Mn, and Co $L_{2,3}$ edges[21]. Figs. 2(a) and (b) show the XPS fit of Ni^{2+} and Mn^{4+} for YNMO samples. The peaks at 855 eV [Fig. 2(a)] and at 642.3 eV [Fig. 2(b)] correspond to the pure Ni^{2+} and Mn^{4+} valence states, respectively. The small sharp peak at 642

eV observed in Fig. 2(b), indicates that there may be a minor Mn^{3+} phase, most likely due to the oxygen vacancies on the particle surfaces and the shoulder at 635 eV is due to Mn-O charge-transfer [22]. The oxidation states for YNCMO sample becomes more complicated with the addition of Co. Figs. 2(c), (d) and (e) display the spectra for Ni, Co, and Mn $L_{2,3}$ edges, respectively. For the Ni $L_{2,3}$ edge, the data shows the best fit for the combination of 67% Ni^{2+} and 33% Ni^{3+} ionic states. At the Co edge, the best fits were achieved for 73% Co^{3+} and 27% Co^{2+} . The small peak above 800 eV in Co-edge is attributed to the Co-O charge transfer [8]. Similarly, for the Mn $L_{2,3}$ -edge, the fit was obtained with 73% Mn^{4+} and 27% Mn^{3+} , where the shoulder at 642 eV is more defined.

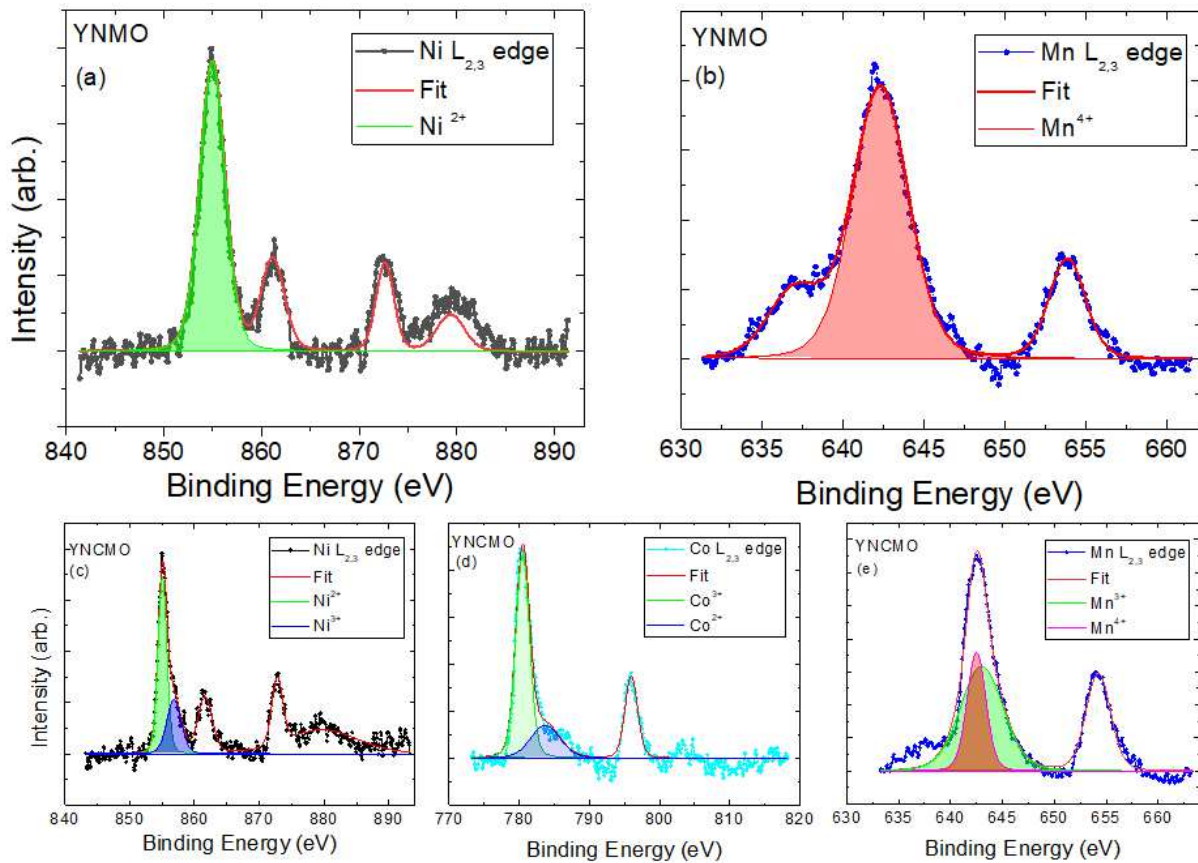


Figure 2 XPS spectra of YNMO sample at (a) Ni and (b) Mn $L_{2,3}$ edges. XPS spectra of YNCMO sample at (c) Ni, (d) Co and (e) Mn $L_{2,3}$ edges.

The powder nature of the samples and the small probe depth ($< 5\text{nm}$) of the experiment, can lead to excess broadening of the peaks and potential oxygen vacancies at particle surfaces which were unaccounted for. Hence, all the acquired fit values should be treated nominally.

3.2 DC magnetization

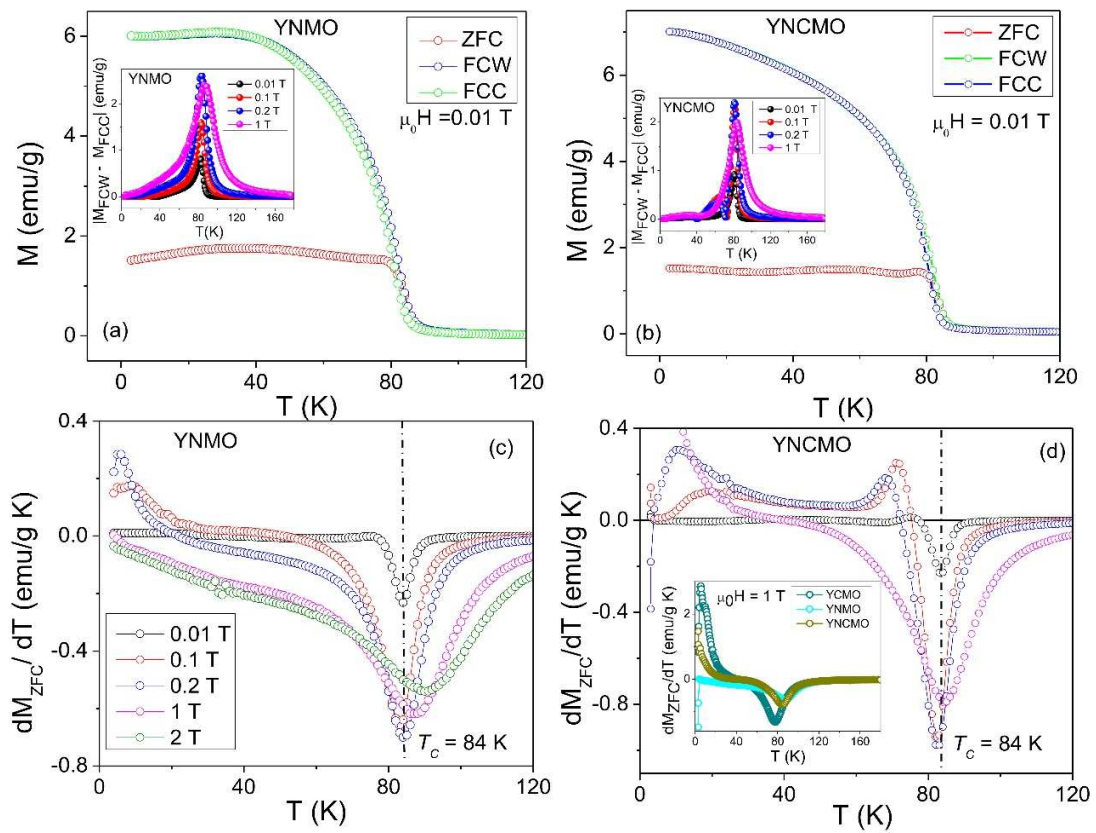


Figure 3 Temperature dependence of the magnetization under zero-field-cooled (ZFC), field-cooled-warming (FCW) and field-cooled-cooling (FCC) protocols for (a) YNMO and (b) YNCMO samples. The insets of (a) and (b) show the magnitude of the difference between FCC and FCW M - T curves at several fields for YNMO and YNCMO, respectively. dM_{ZFC}/dT for the ZFC M - T data at several fields for YNMO (c) and YNCMO (d). A comparison of dM_{ZFC}/dT at $\mu_0 H = 1\text{ T}$ for YCMO, YNMO, and YNCMO is shown in the inset of (d).

The temperature dependent magnetization curves, under three different protocols: zero-field-cooled (ZFC), field-cooled-warming (FCW), and field-cooled-cooling (FCC) for $T = 3 - 120$ K and $\mu_0H = 0.01$ T are shown in Figs. 3(a) and (b) for YNMO and YNCMO, respectively. A clear bifurcation is seen between ZFC and field-cooled (FC) curves below $T = 80$ K for both YNMO and YNCMO. A large separation between the ZFC and FC magnetization at low temperature is observed, which has been previously assigned to the magnetic frustrations in the isostructural compounds [8]. The thermal hysteresis effect has been accentuated by plotting the absolute difference between the FCW and FCC magnetization. The $|M_{\text{FCC}} - M_{\text{FCW}}|$ vs. T for $\mu_0H = 0.01 - 1$ T [refer to the inset of Figs. 3(a) and (b)] reflect maximum hysteresis close to the transition temperature for both the systems. The presence of the thermal hysteresis suggests during the PM – FM phase transition, both, YNMO and YNCMO behave differently upon heating and cooling, indicating the occurrence of competitive magnetic interactions in these systems [23]. The first order differentiation of the ZFC with respect to the temperature for different external magnetic fields is shown in Figs. 3(c) and (d) for YNMO and YNCMO, respectively. The minima in dM_{ZFC}/dT vs. T curve for $\mu_0H = 0.01$ T is used to define the PM – FM phase transition in these systems. For both, YNMO and YNCMO, the $T_C \sim 84$ K, which is higher than the $T_C \sim 76$ K for YCMO [16]. The T_C for a given double perovskite with same R^{3+} ion can be increased by replacing the Co^{2+} with the Ni^{2+} ions. This trend can be seen in isostructural LCMO and LNMO where the T_C changes from 228 K (LCMO) [8] to 280 K (LNMO) [20], which indicates that Ni^{2+} ions give more magnetic stability. It is well known that the structural stability of double perovskites is defined by the Goldschmidt tolerance factor, $t = \frac{r_A + r_O}{\sqrt{2}(r_B + r_O)}$, where r_A , r_B and r_O are the atomic radii of A , an average of B -cations and O , respectively [1]. For the double perovskites with same r_A , the value of t is dependent on the r_B .

The ionic radius of $\text{Ni}^{2+} = 69$ pm and Co^{2+} is 72 pm [24], which gives the tolerance factor of 0.867, 0.874 and 0.871 for YCMO, YNMO and YNCMO, respectively. The YNMO and YNCMO having slightly higher value of t compared to YCMO makes their structure more stable and gives rise to higher T_C . Moreover, T_C is the measure of the strength of FM coupling, and since YNMO has a higher T_C , it can be concluded that $\text{Mn}^{4+}\text{-O}^{2-}\text{-Ni}^{2+}$ is coupled more strongly than $\text{Mn}^{4+}\text{-O}^{2-}\text{-Co}^{2+}$. The non-negative value of dM_{ZFC}/dT seen in Figs 3(c) and (d) is the contribution from the AFM coupling. From the figures it is noted that for YNMO only a small component of $dM_{\text{ZFC}}/dT > 0$ for low fields is seen, while at $\mu_0H > 0.2$ T there is only negative component in the dM_{ZFC}/dT vs. T [Fig. 3(c)]. On the contrary, the maxima in YNCMO starts below T_C for low fields and continues up to 1 T in the low temperature regime [Fig. 3(d)]. A comparison between the dM_{ZFC}/dT vs. T curves at $\mu_0H = 1$ T for YNMO, YNCMO and YCMO is presented in the inset of Fig. 3(d). Based on the consideration that the Co^{2+} ions introduce more defects in the system compared to Ni^{2+} [20], it is anticipated that $dM_{\text{ZFC}}/dT > 0$ persists down to low temperature for the Co-based system and has a higher magnitude for YCMO. The existence of the larger valence fluctuations in the YCMO compared to the YNMO is the possibility for the difference in magnetic behavior observed in these compounds [19]. The Ni^{2+} ions are more stable, leading to the dominant $\text{Mn}^{4+}\text{-O}^{2-}\text{-Ni}^{2+}$ interactions in YNMO, whereas the Co^{2+} ions are comparatively less stable, giving rise to multiple magnetic interactions in YCMO [19]. Furthermore, the XPS data confirms the electronic states of Ni and Mn in YNMO to be 2+ and 4+, suggesting the following possible interactions in the system: $\text{Mn}^{4+}\text{-O}^{2-}\text{-Ni}^{2+}$ (FM), $\text{Ni}^{2+}\text{-O-Ni}^{2+}$ (AFM) and $\text{Mn}^{4+}\text{-O-Mn}^{4+}$ (AFM). The former is the dominant interaction responsible for the FM behavior, and the latter are the consequences of the antiphase boundaries, which is not very significant as observed from the dM_{ZFC}/dT vs. T data. On the other hand, in YNCMO, Ni,

Co and Mn have $2+/3+$, $2+/3+$ and $4+/3+$ states, respectively. The presence of Ni and Co both and two different electronic states gives possibility for multiple magnetic interactions such as $\text{Mn}^{4+}\text{-O}^{2-}\text{-Ni}^{2+}$ (FM), $\text{Mn}^{4+}\text{-O}^{2-}\text{-Co}^{2+}$ (FM), $\text{Mn}^{3+}\text{-O}^{2-}\text{-Ni}^{3+}$ (FM), $\text{Mn}^{3+}\text{-O}^{2-}\text{-Co}^{3+}$ (FM), $\text{Ni}^{2+}\text{-O-Ni}^{2+}$ (AFM), $\text{Mn}^{4+}\text{-O-Mn}^{4+}$ (AFM), $\text{Co}^{2+}\text{-O-Co}^{2+}$ (AFM), $\text{Ni}^{3+}\text{-O-Ni}^{3+}$ (AFM), $\text{Mn}^{3+}\text{-O-Mn}^{3+}$ (AFM), $\text{Co}^{3+}\text{-O-Co}^{3+}$ (AFM) etc. suggesting YNCMO to exhibit competing interactions but with predominant FM coupling. In addition, on the basis of only one PM – FM transition seen in YNCMO two conclusions can be drawn: 1) the uniform distribution of $\text{Ni}^{2+}/\text{Co}^{2+}$ ions in YNCMO; signifying that equal block of $\text{Mn}^{4+}\text{-O}^{2-}\text{-Ni}^{2+}$ interactions have been replaced by $\text{Mn}^{4+}\text{-O}^{2-}\text{-Co}^{2+}$. In a situation where Co^{2+} ions aggregate together in a cluster, an inhomogeneous system with two FM transitions is obtained [25]. 2) There is very little contribution from the $3+$ ionic states of the Ni/Co and Mn ions, else another FM transition is ought to be observed.

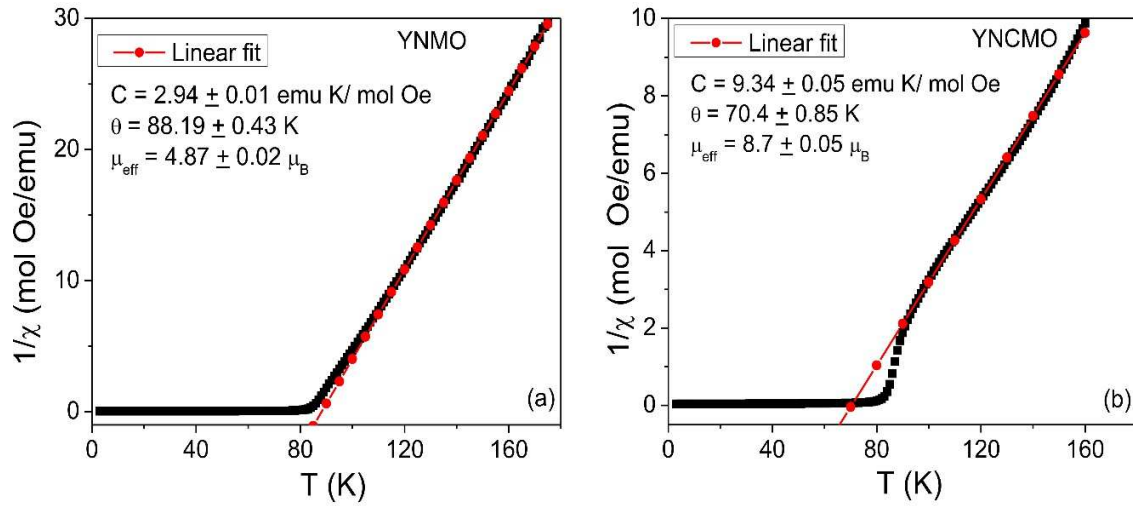


Figure 4 The Curie-Weiss fit of DC susceptibility in the paramagnetic phase for (a) YNMO and (b) YNCMO samples.

The Curie-Weiss fit, $1/\chi = (T - \theta)/C$, of the FCW data for $\mu_0 H = 0.01$ T and $T = 100 - 160$ K is shown in Fig. 4. The fitting parameters were obtained to be $\theta = 88.19 \pm 0.43$ K, $C = 2.94 \pm 0.01$ emu K/mol Oe and paramagnetic susceptibility, $\mu_{eff} = 4.87 \pm 0.02 \mu_B$, and $\theta = 70.40 \pm 0.85$ K, $C = 9.34 \pm 0.05$ emu K/mol Oe and $\mu_{eff} = 8.70 \pm 0.05 \mu_B$, for YNMO [Fig. 4(a)] and YNCMO [Fig. 4(b)], respectively. The positive values of θ for both the compounds further confirms ferromagnetism. The theoretical value of paramagnetic susceptibility, μ_{theo} can be calculated from $\mu_{theo} = \sqrt{\mu_B^2 [g^2 x s(s+1)_{Ni} + g^2 (1-x)s(s+1)_{Co} + g^2 s(s+1)_{Mn}]}$, for $s = 1$ for Ni^{2+} , $3/2$ for Co^{2+} and Mn^{4+} and $x = 1$ for YNMO and 0.5 for YNCMO, $\mu_{theo} = 4.8 \mu_B$ for YNMO and $5.15 \mu_B$ for YNCMO. The $\mu_{eff} \sim \mu_{theo}$ for YNMO while $\mu_{eff} > \mu_{theo}$ for YNCMO. The downward deviation in the $1/\chi$ vs. T curve just above the T_C seen in YNCMO [Fig. 4(b)] points to the existence of the short-range correlated clusters [25] and thus $\mu_{eff} > \mu_{theo}$ in YNCMO system can be associated with the presence of the FM correlations in the PM regime.

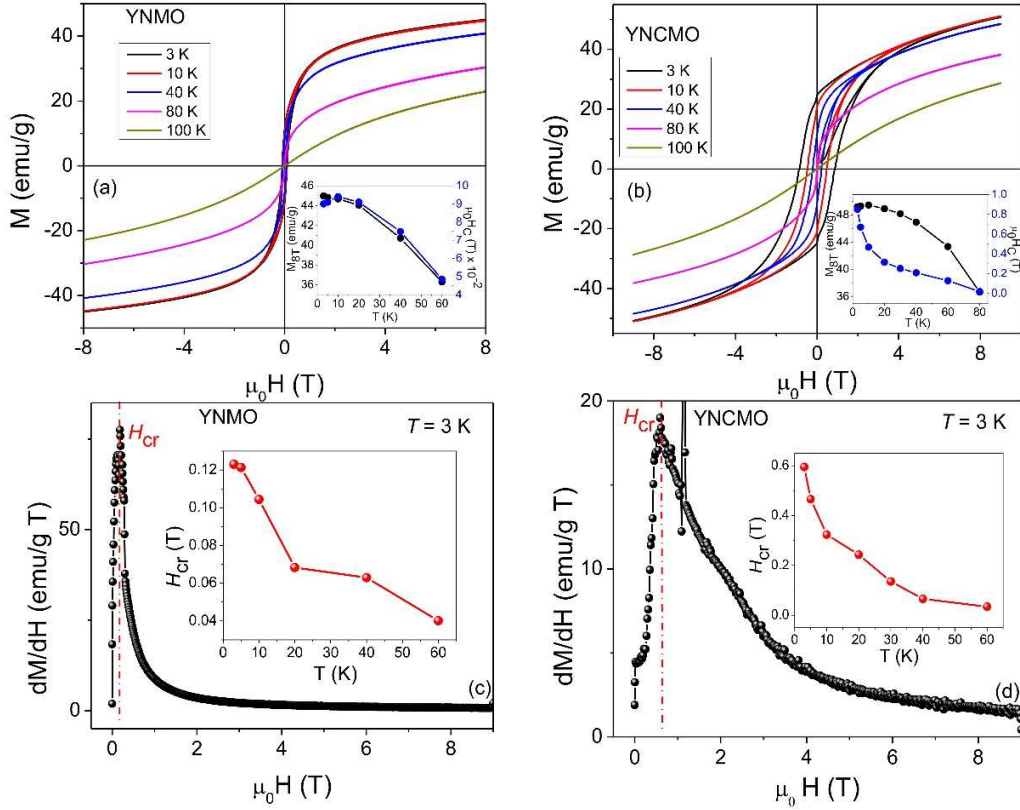


Figure 5 Magnetization versus magnetic field, M vs. H , at several temperatures for (a) YNMO and (b) YNCMO samples. Insets of (a) and (b) show the temperature dependence of coercive field (H_c) and magnetization at $H = 8$ T (M_{8T}). Differential susceptibility (dM/dH) at $T = 3$ K has been shown in (c) and (d) for YNMO and YNCMO, respectively, and their insets show the temperature dependence of H_{cr} for the corresponding samples.

Fig. 5 illustrates the field dependent magnetization curves, M vs. H , for $T = 3 - 100$ K. The magnetic hysteresis loops of the YNMO system [Fig. 5(a)] reflects the soft FM behavior. On doping YNMO with 50 % cobalt, it changes to a hard FM compound [see Fig. 5(b) for YNCMO]. The magnetization at $\mu_0 H = 8$ T and $T = 3$ K is calculated to be $M_{8T} = 3.12 \mu_B/f.u.$ and $3.43 \mu_B/f.u.$ for YNMO and YNCMO, respectively. The magnetic moment for a fully saturated Ni/Mn lattice is theoretically expected to be $5 \mu_B/f.u.$ while that for 0.5 Ni/ 0.5 Co/Mn lattice it is estimated to be $5.52 \mu_B/f.u.$ [using $\mu_{sat} = \sqrt{x(\mu_{sat}^{YCMO})^2 + (1-x)(\mu_{sat}^{YNMO})^2}$, with x

= 0.5]. The low experimental value of M_{8T} can be associated with the antisite defects and oxygen vacancies. In the present case, the lack of saturation in YNMO compound is most likely attributed to the presence of spin canting rather than the antisite defects which have a low contribution to the total signal. For YNCMO, both defects and oxygen vacancies leading to the formation of 3+ ionic states of Ni, Co, and Mn, which were not considered in the calculations and could possibly contribute to the low saturation magnetization. The decrease of M_{8T} and coercive field, H_C , with increasing temperature, which is a feature for a typical FM system, is demonstrated in the insets of Figs. 5(a) and (b). Based on $H_C = 0.09$ T for YNMO and $H_C = 0.85$ T for YNCMO at $T = 3$ K and the nature of M vs. H curve, it can be concluded that the introduction of Co ions in YNMO, makes the system highly anisotropic.

To further compare the antisite defects present in YNMO and YNCMO compounds, we have analyzed the derivatives of the virgin loops. The field dependence of differential susceptibility (dM/dH) at $T = 3$ K is shown in Figs. 5(c) and (d) for YNMO and YNCMO, respectively. A dominant peak at a critical field (H_{cr}) in dM/dH is observed. A peak in dM/dH vs. H curve is usually a signature of a metamagnetic transition [16], however, any sudden change in the net magnetization can also give rise to a prominent peak in differential susceptibility. In the present scenario, this spontaneous change is due to the depinning of the antiphase boundaries/antisite defects in the presence of external magnetic field similar to the case of YCMO [16]. The critical field required for the depinning at $T = 3$ K is very small for YNMO ($H_{cr} = 0.12$ T) compared to that of YNCMO ($H_{cr} = 0.6$ T), which indicates that the AFM coupling in YNMO is weaker. The temperature dependence of H_{cr} is plotted in the insets of Figs. 5(c) and (d), reflecting the decrease in the critical fields with the increase in the temperature.

3.3 AC magnetization

AC magnetic susceptibility is a useful tool for the detection and characterization of any magnetic frustrations present in a given magnetic system. It is the measure of the differential dM/dH response of the system to the time dependent magnetic field, e.g., $H_{AC} = h \sin(2\pi f t)$. Fig. 6 shows the result of AC measurements at frequencies, $f = 10 - 635$ Hz and $T = 10 - 120$ K with an AC driving field amplitude $h = 5$ Oe. Similar to the earlier reports [10], the real part of AC susceptibility, χ' , reflects only one prominent feature close to the T_C for YNMO [Fig. 6(a)]. For consistency with the DC results, the inflection point of χ' is considered as T_C [see the inset (i) of Fig. 6(a)]. The magnitude of the peaks in χ' increases with the increase in the frequency, however, no longitudinal shift along the temperature axis is observed. The presence of frequency *independent* peaks suggest only FM interactions. The inset (ii) of Fig. 5(a) represents the imaginary part of AC- χ , χ'' at $f = 60$ Hz, which further shows the contribution only at PM – FM transition, and remains close to zero at low temperature. χ'' as a function of temperature and frequency is summarized in a surface plot for $f = 10 - 550$ Hz and $T = 10 - 120$ K [Fig. 6(b)]. The warm colors signify the non-zero χ'' . From the Fig. 6(b), it is observed that the significant *loss* for all measured frequencies is seen only at T_C , everywhere else its value is close to zero. In general, χ'' also known as magnetic absorption, is the result of the losses arising from the irreversible magnetization processes like irreversible movement of the domain walls and small hysteresis loops in the FM [26]. Its dominance only at T_C indicates that except for the PM – FM phase transition, no other significant irreversible magnetization process is taking place in YNMO at low DC field.

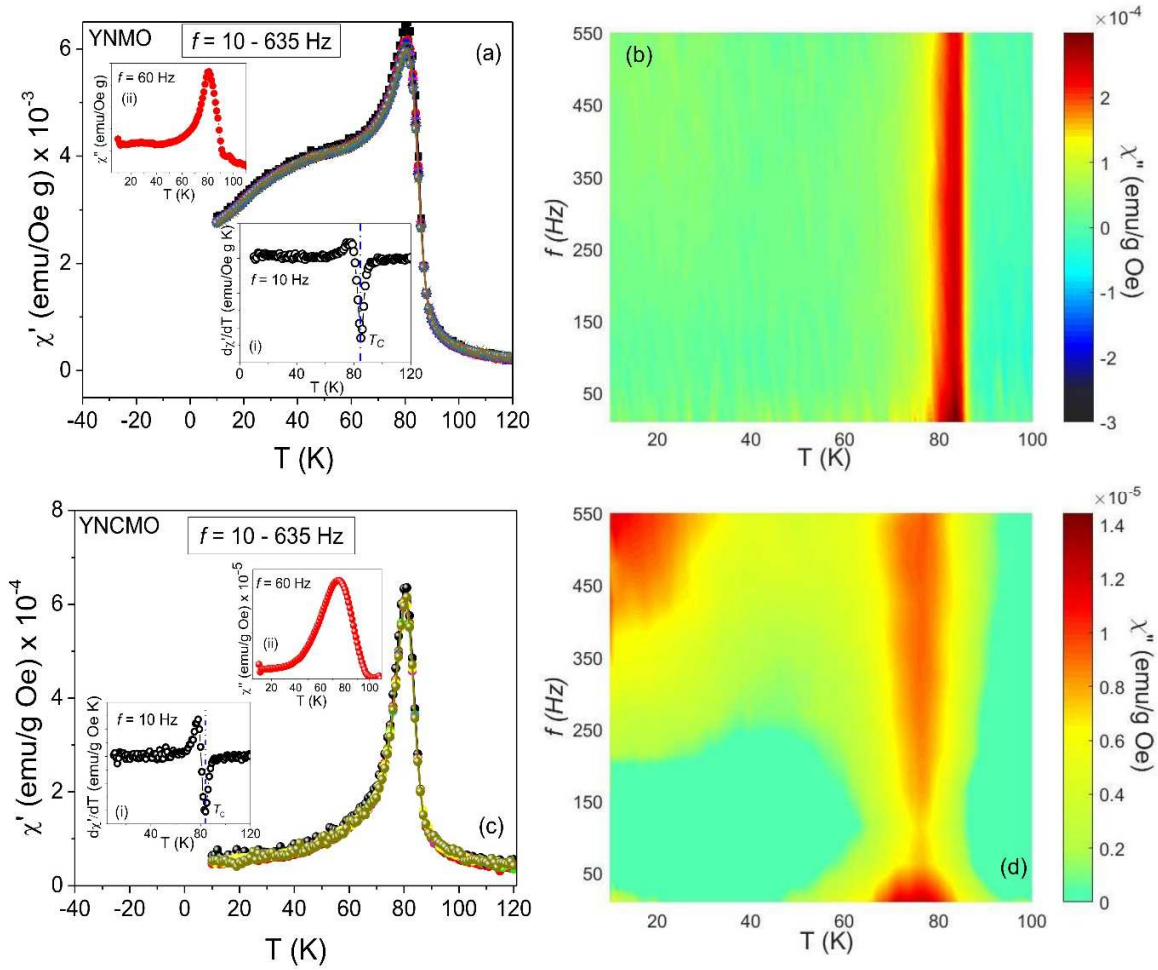


Figure 6 Temperature dependence of real (χ') and imaginary (χ'') part of AC susceptibility. (a) and (c) show χ' vs. T at several frequencies for YNMO and YNCMO, respectively. Insets (i) and (ii) of (a) and (c) represents $d\chi'/dT$ vs. T for frequency (f) = 10 Hz and χ'' vs. T for $f = 60$ Hz, respectively. Surface plot of $\chi''(f, T)$ for YNMO and YNCMO has been shown in (b) and (d), respectively.

Fig. 6(c) and (d) illustrates the χ' and χ'' for YNCMO system. Similar to YNMO, no frequency dependent behavior is observed in the peaks seen in χ' suggesting the presence of only FM interactions close to the PM – FM transition. The inflection point in χ' for $f = 10$ Hz further confirms the T_C observed in the DC magnetization [see the inset (i) of Fig. 6(c)]. The inset (ii) of Fig. 6(c) shows the magnetic absorption at $f = 60$ Hz, having the dominant peak close to T_C . The

surface plot $\chi''(T, f)$ [Fig. 6(d)] outlines the result for the imaginary component. The zero and non-zero value of χ'' is represented by the dark and colored portion of the plot, respectively. Unlike YNMO, as the frequency is increased beyond 200 Hz, a notable χ'' is observed at low temperatures as well, whose magnitude rises with further increase in the frequency. The remarkable low temperature loss at higher frequencies can be associated with the irreversible dynamics of the pinned domain walls in YNCMO at the antiphase boundaries. The presence of antiphase boundaries result in the pinning of domain walls whose slow movement has been detected previously in the magnetic dispersion data [27]. However, in the present case the irreversible relaxation process of the domain walls is probed at a critical frequency and appears as a loss component of AC- χ .

3.4 Magnetic phase diagram

While the magnetocaloric effect (MCE) has been extensively investigated during the last decades for energy-efficient magnetic refrigeration [29-30], it has also been employed as a fundamental probe of magnetic phases' coexistence and conversion, leading to the more comprehensive magnetic phase diagrams established for exotic magnetic systems [8][16][31-34]. MCE is defined as the change in the temperature or entropy of the magnetic material on subjecting it to an external magnetic field adiabatically or isothermally, respectively. The isothermal magnetic entropy (ΔS_M) for a material is calculated by implementing the following Maxwell equation:

$$\left(\frac{\partial S_M(T, H)}{\partial H} \right)_T = \mu_0 \left(\frac{\partial M(T, H)}{\partial T} \right)_H \quad (1)$$

From this we can obtain the analytical form of ΔS_M as follows:

$$\Delta S_M = \mu_0 \int_{H_i}^{H_f} \left(\frac{\partial M}{\partial T} \right) dH \quad (2)$$

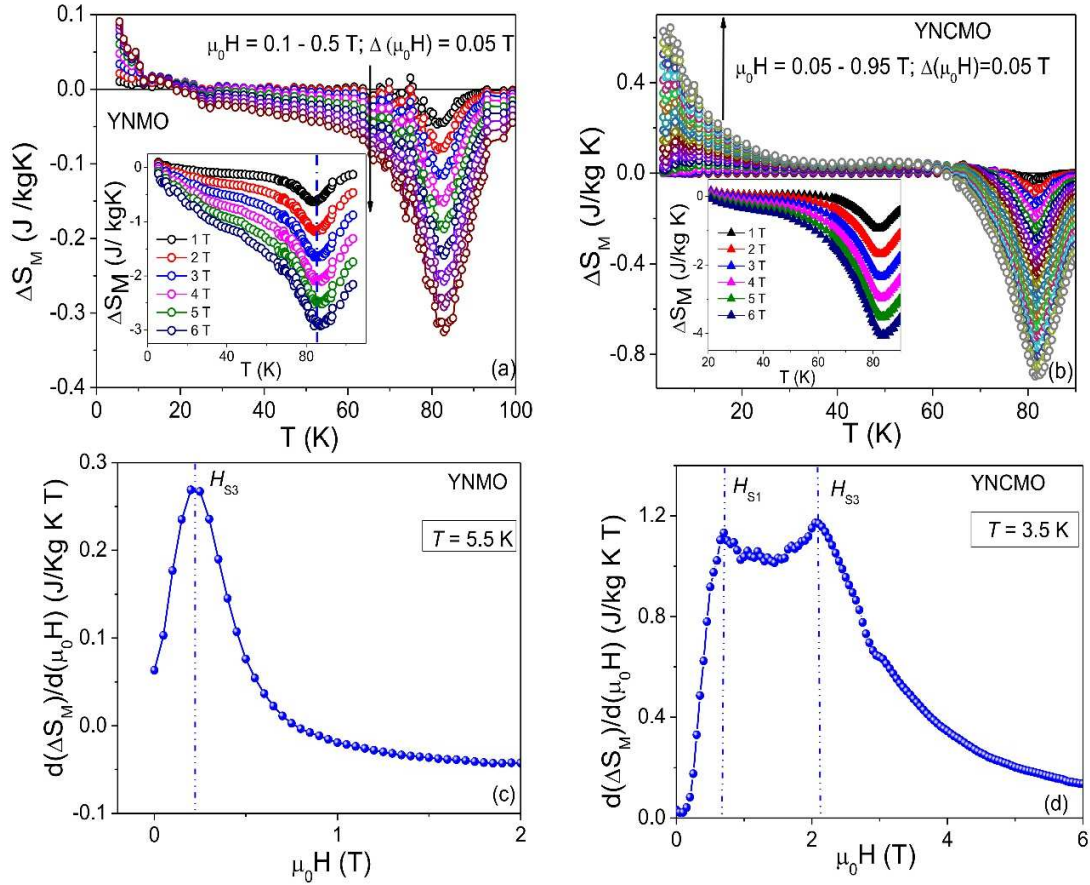


Figure 7 The magnetic entropy change (ΔS_M) (a) and (b) as a function of temperature at low applied magnetic fields; inset (i) shows $\Delta S_M(T, \mu_0 \Delta H)$ curves at high field for YNMO and YNCMO samples, respectively. (c) and (d) show the $d\Delta S_M/dH$ vs. H curve at $T = 5.5$ K for YNMO and $T = 3.5$ K for YNCMO systems.

From equation (2) the direct relation between ΔS_M and dM/dT , suggests that ΔS_M is intrinsically sensitive to the magnetic transitions and the region of spontaneous change in the magnetization and hence any maxima or minima observed in ΔS_M vs. T curves can be attributed to the phase

transitions. A conventional PM – FM phase transition will exhibit $\Delta S_M < 0$, as the Zeeman energy suppresses the thermal fluctuations of the spin system [8][16]. However, for an inverse MCE, $\Delta S_M > 0$ is observed. Such an increase in entropy with magnetic field is typically assigned to the AFM coupling [8][16]. In general, $\Delta S_M > 0$ is seen when the external magnetic field induces spin disorder in the process of aligning the spins along the field direction and against their zero-field spin configuration. In the following, the change in magnetic entropy as a function of temperature and field is analyzed across the phase diagram for YNMO and YNCMO systems.

The isotherms M vs. H were measured using warming protocol for $T = 3 - 100$ K and $3 - 90$ K for YNMO and YNCMO, respectively, for $\mu_0 H = 0 - 6$ T. Fig. 7 demonstrates the magnetic entropy data for YNMO and YNCMO. ΔS_M vs. T for $\mu_0 \Delta H = 0.1 - 0.5$ T for YNMO is shown in Fig. 7(a). The dominant minima at T_C represents the transition from disordered PM phase to an ordered FM. The small non-negative value at $T < 20$ K for low fields can be associated with the existence of AFM interactions. $\Delta S_M > 0$ has also been previously assigned to antiferromagnetism in similar compounds, YCMO [16] and LCMO [8]. With the increase in the magnetic field, the positive ΔS_M contributions shift to lower temperature, and eventually completely suppressed. A similar ΔS_M vs. T behavior is observed for YNCMO as well. Fig. 7(b) shows the ΔS_M vs. T curve for $\mu_0 \Delta H = 0.05 - 0.95$ T for YNCMO, with the most prominent minima at T_C , as a signature of a PM – FM phase transition. Compared to YNMO [Fig. 7(a)], more significant positive ΔS_M is observed at low temperatures. For $T < 20$ K, $\Delta S_M > 0$ for the maximum applied field, indicating the presence of strong AFM coupling in YNCMO. From Fig. 7 it can also be noted that the crossover temperature from AFM – FM regime decreases with the increase in external magnetic field for both, YNMO and YNCMO, specifying field induced disorder. The insets of Figs. 7(a) and (b) further shows that the PM – FM transition temperature remains constant irrespective of

the magnitude of the external magnetic field. The change in ΔS_M with respect to the magnetic field ($d\Delta S_M/d\mu_0\Delta H$) has been plotted in Figs. 7(c) and (d). The occurrence of a peak in $d\Delta S_M/d\mu_0\Delta H$ vs. μ_0H would justify any abrupt change in ΔS_M , which is further related to sudden change in the magnetization. Fig. 7(c) shows $d\Delta S_M/d\mu_0\Delta H$ vs. μ_0H at $T = 5.5$ K for YNMO with a single peak, named as H_{S3} . Meanwhile, for YNCMO [Fig. 7(d)] two different peaks are observed in $d\Delta S_M/d\mu_0\Delta H$ vs. μ_0H at $T = 3.5$ K, similar to that of YCMO [16]. Apart from H_{S3} , H_{S1} is also marked at lower fields. The rise of $d\Delta S_M/d\mu_0\Delta H$ at certain critical field implies ΔS_M does not behave the same for all magnetic fields in $Y_2Ni_xCo_{1-x}MnO_6$ compounds. Moreover, the peak shifts towards higher fields when Co^{2+} concentration is increased.

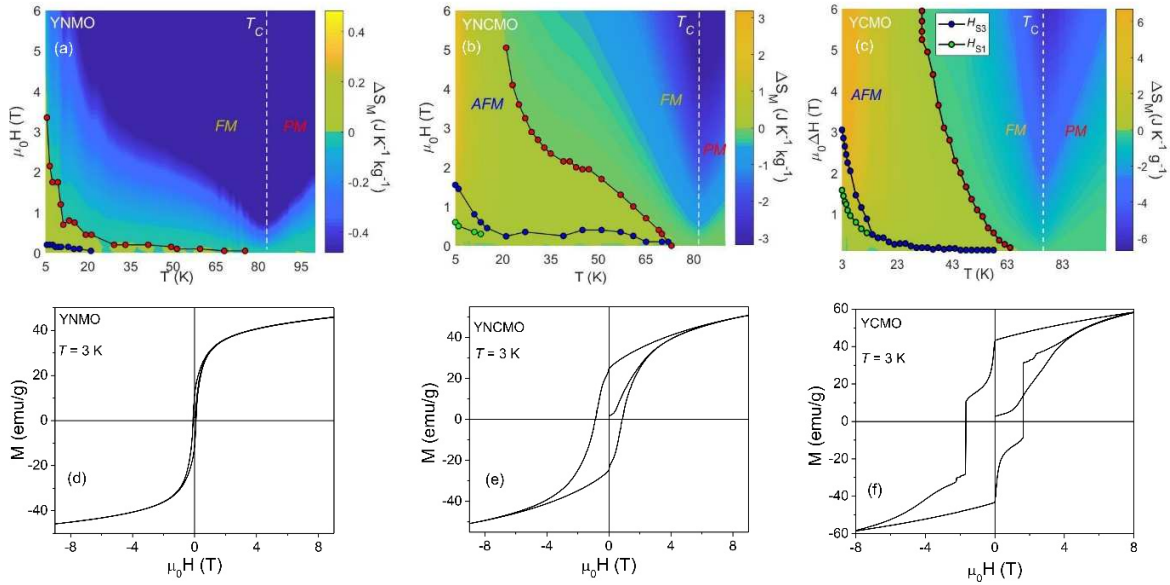


Figure 8 The H - T phase diagram of the monoclinic $P2_1/n$ Y_2NiMnO_6 (a), $Y_2Ni_{0.5}Co_{0.5}MnO_6$ (b) and Y_2CoMnO_6 (c). The surface plot shows ΔS_M over a full range of temperatures for different magnetic field changes. $T = T_C$ (the dashed white line) marks the PM-FM phase transition. The critical fields for the dominant FM region are marked with the dashed black lines. The blue (H_{S1}) and green (H_{S3}) circles mark the peaks in the $d\Delta S_M/dH$ vs. H curves. The red circles denote the separation between AFM and FM regime. (d), (e), and (f) represent the M vs. H at $T = 3$ K for YNMO, YNCMO, and YCMO, respectively

A detailed magnetic phase diagram as functions of magnetic field and temperature has been summarized in Fig. 8 for YNMO [Fig. 8(a)] and YNCMO [Fig. 8(b)] and is compared with the previously established magnetic phase diagram of YCMO [Fig. 8(c)] [13]. The constructed phase diagrams clearly predict the effect of doping in $Y_2Ni_xCo_{1-x}MnO_6$ for $x = 1, 0.5$ and 0 and show how different concentrations of Co can alter the magnetism in $Y_2Ni_xCo_{1-x}MnO_6$. In Figs. 8(a) and (b), the phase evolution of YNMO and YNCMO can be seen from the dominant PM – FM at high temperature, demarcated by the white dashed line (T_C), to the FM – AFM at a low temperature. In all three surface plots, the region below the red circles represent the area where the external magnetic field increases the change in magnetic entropy, $\Delta S_M > 0$, while the area above it signifies the region of lower magnetic entropy change, $\Delta S_M < 0$. The features observed in the $d\Delta S_M/d\mu_0\Delta H$ vs. μ_0H curve, H_{S3} and H_{S1} , are shown with the help of blue and green circles. In YNMO [Fig. 8(a)], a sharp drop in the critical field from 3.5 T at 5 K to less than 0.5 T at 20 K is observed for non-negative ΔS_M (follow the red circles), while positive ΔS_M remains up to 6 T for $T < 20$ K in YNCMO [Fig. 8(b)] and continues up to $T < 33$ K for YCMO [Fig. 8(c)]. The persistence of AFM interactions ($\Delta S_M(\mu_0\Delta H, T) > 0$) up to higher fields and higher temperature with the increase in Co^{2+} ionic concentration suggests cobalt induced AFM coupling in $Y_2Ni_xCo_{1-x}MnO_6$. As mentioned earlier, the antiferromagnetism in these systems arise due to the formation of the antiphase boundaries, and since Co^{2+} results in more disorder compared to Ni^{2+} , the AFM regime and the strength of interactions increases with Co concentration. The AFM ordering at the phase boundaries pins the domain walls and certain critical field is required to de-pin and orient the spins along the external field direction. The orientation of spins lead to spontaneous change in magnetization at the critical fields (H_{S3} and H_{S1}). The magnitude of H_{S3} at

$T = 5$ K is 0.2 T, 1.55 T and 2.25 T for YNMO, YNCMO and YCMO, respectively, which further supports the presence of strongest antiparallel coupling in YCMO. Figs. 8(d), (e) and (f) differentiates between the M vs. H loop of magnetic systems under consideration at $T = 3$ K. In $Y_2Ni_xCo_{1-x}MnO_6$, the compound changes from a soft FM to a hard FM compound with high magnetocrystalline anisotropy, when x takes the value 1, 0.5 and 0. The antiphase boundaries introduced by Co^{2+} ions, is reflected as a metamagnetic behavior in these compounds.

4. Conclusion

A magnetic study on $Y_2Ni_xCo_{1-x}MnO_6$ compounds for $x = 1, 0.5$ was conducted and the results were compared with the pre-existing YCMO. The polycrystalline samples of YNMO and YNCMO synthesized via *sol-gel* technique yielded single monoclinic ($P2_1/n$) phase with only Ni^{2+}/Mn^{4+} and mixed $Ni^{2+/3+}/Co^{2+/3+}/Mn^{4+/3+}$ cationic ordering in YNMO and YNCMO, respectively. The occurrence of single peak in M vs. T curve in YNCMO confirms the homogeneous replacement of Ni^{2+} ions by Co^{2+} . The temperature dependent magnetization results further suggest the presence of weak AFM interactions at low temperature in YNMO compared to YNCMO and YCMO. The *loss* in AC susceptibility at low temperature signifies the domain wall motion in the case of YNCMO which is completely absent in YNMO. The MCE measurements helped to establish the phase diagram to understand the evolution and stabilization of AFM and FM phases in these compounds. From the study, it was understood that in YNMO, the most dominant interaction is $Mn^{4+}-O^{2-}-Ni^{2+}$, the AFM interactions have very small contribution. The AFM coupling among $Y_2Ni_xCo_{1-x}MnO_6$ compounds becomes stronger and is thermally favored at low temperature with the addition/increase of Co^{2+} concentration.

Acknowledgments

Research at USF was supported by the U.S. Department of Energy, Office of Basic Energy Sciences, Division of Materials Sciences and Engineering under Award No. DE-FG02-07ER46438.

References

- [1] L. Li, P. Xu, S. Ye, Y. Li, G. Liu, D. Huo and M. Yan, Magnetic properties and excellent cryogenic magnetocaloric performances in B-site ordered $\text{RE}_2\text{ZnMnO}_6$ (RE = Gd, Dy and Ho) perovskites, *Acta Mater.*, 194 (2020) 354-365.
- [2] B. Yu, Y. Zhang, D. Guo, J. Wang, and Z. Ren, Structure, magnetic properties and cryogenic magneto-caloric effect (MCE) in $\text{RE}_2\text{FeAlO}_6$ (RE = Gd, Dy, Ho) oxides, *Ceram. Int.*, 47 (2021) 6290-6297.
- [3] P. Xu, Z. Ma, P. Wang, H. Wang, and L. Li, Excellent cryogenic magnetocaloric performances in ferromagnetic $\text{Sr}_2\text{GdNbO}_6$ double perovskite compound, *Mater. Today Phys.*, 20 (2021) 100470.
- [4] S. Vasala and M. Karppinen, $\text{A}_2\text{B}'\text{B}''\text{O}_6$ perovskites: A review, *Prog. Solid State Chem.*, 43 (2015) 1–36.
- [5] M. Nasir, S. Kumar, N. Patra, D. Bhattacharya, S. Nath Jha, Dharma R. Basaula, Subhash Bhatt, Mahmud Khan, Shun-Wei Liu, Sajal Biring, and Somaditya Sen, Role of antisite disorder, rare-earth size, and superexchange angle on band gap, Curie temperature, and magnetization of R_2NiMnO_6 double perovskites, *Appl. Electron. Mater.*, 1 (2019) 141–153.
- [6] María Retuerto, Ángel Muñoz, María Jesús Martínez-Lope, José Antonio Alonso, Federico J. Mompeán, María Teresa Fernández-Díaz, and Javier Sánchez-Benítez,

- Magnetic interactions in the double perovskites R_2NiMnO_6 ($R = Tb, Ho, Er, Tm$) investigated by neutron diffraction, *Inorg. Chem.*, **54** (2015) 10890–10900.
- [7] M. P. Singh, K. D. Truong, and P. Fournier, Magnetodielectric effect in double perovskites La_2CoMnO_6 , *Appl. Phys. Lett.*, **91** (2007) 042504.
- [8] R. P. Madhugaria, R. Das, E. M. Clements, N. T. Dang, D. P. Kozlenko, N. S. Bingham, V. Kalappattil, M. H. Phan, and H. Srikanth, Evidence of long-range ferromagnetic order and spin frustration effects in the double perovskite La_2CoMnO_6 , *Phy. Rev. B*, **99** (2019) 104436.
- [9] Sanjeev Kumar, Gianluca Giovannetti, Jeroen van den Brink, and Silvia Picozzi, Theoretical prediction of multiferroicity in double perovskite in Y_2NiMnO_6 , *Phy. Rev. B*, **82** (2010) 134429.
- [10] R. P. Maiti, S. Dutta, M. Mukherjee, M. K. Mitra and D. Chakravorty, Magnetic and dielectric properties of sol-gel derived nanoparticles of double perovskite Y_2NiMnO_6 , *J. Appl. Phys.* **112** (2012) 044311.
- [11] H. Nhalil, H. S. Nair, C. M. N. Kumar, A. M. Strydom, and S. Elizabeth, Ferromagnetism and the effect of free charge carriers on electric polarization in double perovskite Y_2NiMnO_6 , *Phys. Rev. B* **92** (2015) 214426.
- [12] J. Blasco, J. L. García-Muñoz, J. García, G. Subías, J. Stankiewicz, J. A. Rodríguez-Velamazán, and C. Ritter, Magnetic order and magnetoelectric properties of R_2CoMnO_6 perovskites ($R = Ho, Tm, Yb$ and Lu), *Phy. Rev. B*, **96** (2017) 024409.
- [13] C. Y. Ma, S. Dong, P. X. Zhou, Z. Z. Du, M. F. Liu, H. M. Liu, Z. B. Yana, and J.-M. Liu, The ferroelectric polarization of Y_2NiMnO_6 aligns along b-axis: the first principle calculations, *Phys. Chem. Chem. Phys.*, **17** (2015) 20961-20970.

- [14] J. Blasco, J. García, G. Subías, J. Stankiewicz, J. A. Rodríguez-Velamazán, C. Ritter, J. L. García-Muñoz, and F. Fauth, Magnetolectric and structural properties of Y_2CoMnO_6 : the role of antisite defects, *Phys. Rev. B*, 93 (2016) 214401.
- [15] Chenyang Zhang, Tingsong Zhang, Lei Ge, Shan Wang, Hongming Yuan, and Shouhua Fenga, Hydrothermal synthesis and multiferroic properties of Y_2NiMnO_6 , *RSC Adv.*, 4 (2014) 50969.
- [16] R.P. Madhogaria, E. M. Clements, V. Kalappattil, N.T. Dang, R. Das, N. S. Bingham, D.P.Kozlenko, M.H. Phan and H. Srikanth, Metamagnetism and kinetic arrest in long-range ferromagnetically ordered multicaloric double perovskite Y_2CoMnO_6 , *J. Magn. Mater.*, 507 (2020) 166821.
- [17] J. Su, Z. Z. Yang, X. M. Lu, J. T. Zhang, L. Gu, C. J. Lu, Q. C. Li, J.-M. Liu, and J. S. Zhu, Magnetism-driven ferroelectricity in double perovskite Y_2NiMnO_6 , *Appl. Mater. Interfaces*, 7 (2015) 13260–13265.
- [18] Hari Krishnan S. Nair, R. Pradheesh, Yinguo Xiao, Dona Cherian, Suja Elizabeth, Thomas Hansen, Tapan Chatterji, and Th. Brückel, Magnetization-steps in Y_2CoMnO_6 double perovskite: the role of antisite disorder, *J. Appl. Phys.*, 116 (2014) 123907.
- [19] Vasundhara Katari, Peram Delli Babu, Sanjaya K. Mishra, Ranjan Mittal, Samatha Bevara, Srungarpu N. Achary, Sudhansu K. Deshpande, and Avesh K. Tyagi, Effects of preparation conditions on magnetic and dielectric properties of Y_2MMnO_6 ($M = Co, Ni$), *J. Am. Ceram. Soc.*, **99** (2016) 499–506.
- [20] A. Harbi , H. Moutaabbid , Y. Li, Carlos Renero-Lecuna, M. Fialin, Y. Le Godec ,S. Benmokhtar, M. Moutaabbid, The effect of cation disorder on magnetic properties of new

- double perovskites $\text{La}_2\text{Ni}_x\text{Co}_{1-x}\text{MnO}_6$ ($x = 0.2-0.8$), *J. Alloys Compd.*, **778** (2019) 105-114.
- [21] N. Fairley, A. Carrick, *The Casa Cookbook*, Acolyte Science, Cheshire, U.K. (2005)
- [22] D. Asakura, Y. Nanba, E. Hosono, M. Okubo, H. Niwa, H. Kiuchi, J. Miyawaki, and Y. Harada, Mn 2p resonant X-ray emission clarifies the redox reaction and charge-transfer effects in LiMn_2O_4 , *Phys. Chem. Chem. Phys.* **21** (2019) 18363-18369.
- [24] A. Banerjee, A. K. Pramanik, K. Kumar, and P. Chaddah, Coexisting tunable fractions of glassy and equilibrium long-range-order phases in manganites, *J. Phys.: Condens. Matter*, **18** (2006) L605–L611.
- [25] R. D. Shannon, *Acta Crystallographica*, **32** (1976) 751–767.
- [26] D. Pramanik, S. Mukherjee, S. Dan, A. Nandy, S.K. Pradhan, P. Dasgupta, A. Poddar, M. Mukherjee, B. Manjunath, P.A. Joy, Structural and magnetic properties of $\text{La}_2\text{Ni}_{1-x}\text{Co}_x\text{MnO}_6$ compounds *Mate. Res. Bull.*, **102** (2018) 248–256.
- [27] M. Bałanda, AC susceptibility studies of phase transitions and magnetic relaxation: conventional, molecular and low-dimensional magnets, *Acta Phys. Pol. A*, **124** (2013) 964–976.
- [28] J. K. Murthy and A. Venimadhav, Multicaloric effect in multiferroic Y_2CoMnO_6 , *J. Appl. Phys.*, **47** (2014) 445002.
- [29] L. Li, and M. Yan, Recent progresses in exploring the rare earth based intermetallic compounds for cryogenic magnetic refrigeration, *J. Alloys and Compds.*, **823** (2020) 153810.
- [30] Y. Zhang, Review of the structural, magnetic and magnetocaloric properties in ternary rare earth $\text{RE}_2\text{T}_2\text{X}$ type intermetallic compounds, *J. Alloys and Compds.*, **787** (2019)

1173-1186.

- [31] E. M. Clements, R. Das, L. Li, Paula J. Lampen-Kelley, M.H. Phan, V. Keppens, D. Mandrus, and H. Srikanth, Critical behavior and macroscopic phase diagram of the monoaxial chiral helimagnet $\text{Cr}_{1/3}\text{NbS}_2$, *Sci. Rep.* **7** (2017) 6545.
- [32] M. H. Phan and S.C. Yu, Review of the magnetocaloric effect in manganite materials, *J. Magn. Magn. Mater.* **308** (2007) 325–340.
- [33] P. Lampen, N. S. Bingham, M. H. Phan, H. Srikanth, H. T. Yi, and S. W. Cheong, Macroscopic phase diagram and magnetocaloric study of metamagnetic transitions in the spin chain system $\text{Ca}_3\text{Co}_2\text{O}_6$, *Phys. Rev. B* **89** (2014) 144414.
- [34] N. S. Bingham, A. K. Suszka, C. A. F. Vaz, H. Kim, and L. J. Heyderman, Interfacial room temperature magnetism and enhanced magnetocaloric effect in strained $\text{La}_{0.66}\text{Ca}_{0.34}\text{MnO}_3/\text{BaTiO}_3$ heterostructures, *Phys. Rev. B* **96** (2017) 024419.

Figure Captions

Figure 1: XRD patterns of the polycrystalline (a) YNMO and (b) YNCMO samples. The star represents the peak corresponding to Y_2O_3 .

Figure 2: XPS spectra of YNMO sample at (a) Ni and (b) Mn $L_{2,3}$ edges. XPS spectra of YNCMO sample at (c) Ni, (d) Co and (e) Mn $L_{2,3}$ edges.

Figure 3: Temperature dependence of the magnetization under zero-field-cooled (ZFC), field-cooled-warming (FCW) and field-cooled-cooling (FCC) protocols for (a) YNMO and (b) YNCMO samples. The insets of (a) and (b) show the magnitude of the difference between FCC and FCW M - T curves at several fields for YNMO and YNCMO, respectively. dM_{ZFC}/dT for the

ZFC M - T data at several fields for YNMO (c) and YNCMO (d). A comparison of dM_{ZFC}/dT at $\mu_0H = 1$ T for YCMO, YNMO, and YNCMO is shown in the inset of (d).

Figure 4: The Curie-Weiss fit of DC susceptibility in the paramagnetic phase for (a) YNMO and (b) YNCMO samples.

Figure 5: Magnetization versus magnetic field, M vs. H , at several temperatures for (a) YNMO and (b) YNCMO samples. Insets of (a) and (b) show the temperature dependence of coercive field (H_c) and magnetization at $H = 8$ T (M_{8T}). Differential susceptibility (dM/dH) at $T = 3$ K has been shown in (c) and (d) for YNMO and YNCMO, respectively, and their insets show the temperature dependence of H_{cr} for the corresponding samples.

Figure 6: Temperature dependence of real (χ') and imaginary (χ'') part of AC susceptibility. (a) and (c) show χ' vs. T at several frequencies for YNMO and YNCMO, respectively. Insets (i) and (ii) of (a) and (c) represents $d\chi'/dT$ vs. T for frequency (f) = 10 Hz and χ'' vs. T for $f = 60$ Hz, respectively. Surface plot of $\chi''(f, T)$ for YNMO and YNCMO has been shown in (b) and (d), respectively.

Figure 7: The magnetic entropy change (ΔS_M) (a) and (b) as a function of temperature at low applied magnetic fields; inset (i) shows $\Delta S_M(T, \mu_0\Delta H)$ curves at high field for YNMO and YNCMO samples, respectively. (c) and (d) show the $d\Delta S_M/dH$ vs. H curve at $T = 5.5$ K for YNMO and $T = 3.5$ K for YNCMO systems.

Figure 8: The H - T phase diagram of the monoclinic $P2_1/n$ Y_2NiMnO_6 (a), $Y_2Ni_{0.5}Co_{0.5}MnO_6$ (b) and Y_2CoMnO_6 (c). The surface plot shows ΔS_M over a full range of temperatures for different magnetic field changes. $T = T_C$ (the dashed white line) marks the PM-FM phase transition. The critical fields for the dominant FM region are marked with the dashed black lines. The blue (H_{SI})

and green (H_{S3}) circles mark the peaks in the $d\Delta_S/dH$ vs. H curves. The red circles denote the separation between AFM and FM regime. (d), (e), and (f) represent the M vs. H at $T = 3$ K for YNMO, YNCMO, and YCMO, respectively